Radiation dose reduction in medical CT through equally sloped tomography

Benjamin P. Fahimian[1,2,6], Yunzhe Zhao[1,6], Russell Fung[1], Yu Mao[4], Chun Zhu[1], Zhifeng Huang[1], Maryam Khatonabadi[3], John J. DeMarco[3], Stanley J. Osher[5], Michael F. McNitt-Gray[3] and Jianwei Miao[1*]

[1]*Department of Physics & Astronomy and California NanoSystems Institute, University of California, Los Angeles, CA 90095*

[2]*Department of Radiation Oncology, Stanford University, Stanford, CA 94305*

[3]*Biomedical Physics Interdepartmental Program, David Geffen School of Medicine at UCLA, Los Angeles, CA 90095-1770*

[4]*Institute for Mathematics and Its Applications, University of Minnesota, Mineapolis, MN 55455*

[5]*Department of Mathematics, University of California, Los Angeles, CA 90095*

[6]*These authors contributed equally to this work.*

**miao@physics.ucla.edu*

Purpose: A Fourier-based iterative algorithm, termed equally sloped tomography (EST), in conjunction with advanced regularization methods, has been applied to reduce the radiation dose in medical CT. To quantify the amount of CT dose reduction achievable by EST, image quality phantom and an anonymous pediatric patient data sets were acquired from a Siemens SOMATOM Sensation 64 scanner.

Methods: EST iterates back and forth between real and Fourier space utilizing the pseudo-polar fast Fourier transform (PPFFT). In each iteration, physical constraints and mathematical regularization are enforced in real space, while the measured data is applied in Fourier space. The algorithm, monitored by an error metric, is guided towards a global minimum that is consistent with the measured data. To prevent any human intervention, the algorithm is automatically terminated when no further improvement can be made. Quantitative comparisons are conducted on the filtered back projection (FBP) and EST reconstructions at different flux settings using signal-to-noise ratios (SNRs) and contrast-to-noise ratios (CNRs).

Results: Based on the phantom and anonymous pediatric patient data sets and the image quantification metrics such as SNRs and CNRs, our experimental results demonstrate that the 39mAs EST reconstructions produce comparable or better image quality, resolution and contrast than the 140mAs FBP reconstructions.

Conclusions: As the radiation dose is linearly proportional to the x-ray flux, our results suggest that EST enable a reduction of the CT dose by ~70% while producing comparable or better image quality, contrast and resolution than the conventional reconstruction method. Compared to other iterative algorithms, EST takes advantage of the best features in both real and Fourier space iterative algorithms: i) eliminating the need for interpolation in Fourier space, 2) utilizing the PPFFT that is algebraically exact and computationally fast, and 3) searching for a global minimum using the measured data through an iterative process in conjunction with advanced mathematical regularization. While we demonstrate the radiation dose reduction with fan-beam CT data in this article, EST can also be extended to circular/helical cone-beam geometry through the rebinning process.

Keywords: equally sloped tomography (EST), radiation dose reduction, iterative algorithm, oversampling, pseudopolar fast Fourier transform (PPFFT)

I. INTRODUCTION

Since its inception in the 1970s, X-ray computed tomography (CT) has become a revolutionary medical tool in diagnosis of diseases and visualization of critical interventional procedures[1-3]. However, due to the requirement of sufficiently high flux projections from multiple directions for achieving high quality images, a major concern in medical CT is the unavoidable radiation dose delivered to the patient, especially to the more radiosensitive population such as pediatrics[4-9]. According to the 2009 report from the National Council on Radiation Protection & Measurements[10], CT accounts for about 15% of the total radiological examinations, but is disproportionately responsible for approximately 50% of the medical radiation exposure and nearly 25% of the total population exposure. Recently, the combination of real space iterative algorithms with modern optimization methods has been rapidly developed to reduce radiation dose in CT[11-18]. While these methods perform well under certain circumstances (*i.e.* for piecewise constant objects), partially due to the presence of noise in the CT data as well as limitations in the computation speed, currently the most popular method in clinical CT and other tomographic fields remains filtered back projection (FBP) or its variations[19-20]. In this article, we applied equally sloped tomography (EST)[21-26], a Fourier-based iterative reconstruction algorithm, together with modern optimization methods[24,27-29] to a phantom and an anonymous pediatric patient data set acquired from a Siemens SOMATOM Sensation 64 scanner. Our experimental results from the phantom and the anonymous pediatric patient data sets indicate that EST can reduce the CT dose by ~70%, while producing comparable or better image resolution and contrast than the conventional FBP reconstructions.

II. METHODS

II.A. The Pseudopolar Fast Fourier Transform

Conventional equally-angled acquisitions result in a polar distribution of points, and in order to reconstruct 3D objects in the Cartesian grid, interpolations must be implemented either in real or Fourier space[1-3,20]. Unlike interpolations in real space where the interpolation error is constrained in the neighboring area, interpolations in Fourier space affect the quality throughout the entire image[30-32]. Furthermore, since the radial density of sampling points becomes sparser at higher spatial frequencies in Fourier space, the image is degraded at higher frequencies. Although it is believed that no direct and exact fast Fourier transform algorithm can be constructed between the polar and Cartesian grids[32], it has been shown the existence of an algebraically exact fast Fourier transform algorithm between the pseudopolar and Cartesian grids, termed the pseudopolar fast Fourier transform (PPFFT)[33, 34]. As depicted in Fig. 1, for a $N \times N$ Cartesian grid, the pseudopolar grid is defined by a set of 2N lines, each line consisting of 2N grid points mapped out on N concentric squares. The $2N$ lines are subdivided into two groups. A horizontal group (in gray) is defined by $y = sx$, where s is the slope, $|s| \leq 1$ and Δs is a constant ($2/N$), while a vertical group (in red) is defined by $x = sy$, where $|s| \leq 1$ and Δs is a constant ($2/N$) as well. The horizontal and vertical groups are symmetric under the interchange of x and y. These pseudopolar lines are termed "equally-sloped" since the slope, s, of successive lines in both groups changes by an equal sloped increment of $\Delta s = 2/N$ as opposed to a fixed equal angled increment as in the polar grid. Unlike the polar grid, the distance between sampling points on the individual lines of the pseudopolar grid varies from line to line. The fractional Fourier transform (FrFT) can be used to vary the output sampling distance of the Fourier transform[35]. The 1D FrFT is defined by

$$F_\alpha(k) = \sum_{x=0}^{N-1} f(x) \exp\left(-\frac{i2\pi\alpha kx}{N}\right), \tag{1}$$

This is equivalent to the standard 1D fast Fourier transform but with an extra factor of α in the exponent; by choosing an appropriate value for α, the projection data can be mapped on to the grid points of any line on the pseudopolar grid. Taking the vertical group as an example, the

PPFFT is expressed as

$$F(k_x,k_y)=\sum_{x=0}^{N-1}\left[\sum_{y=0}^{N-1} f(x,y)\exp(-ik_y y)\right]\exp(-\frac{i2mk_y x}{N}) \tag{2}$$

where

$$\left\{k_y=\frac{2\pi l}{N}\right\}_{l=-\frac{N}{2}}^{\frac{N}{2}-1} \quad , \quad \left\{k_x=\frac{2mk_y}{N}\right\}_{m=-\frac{N}{2}}^{\frac{N}{2}-1} \tag{3}$$

Note that the pseudopolar grid and the PPFFT algorithm were originally developed to interpolate tomographic projections from the polar to the Cartesian grid in reciprocal space[33, 34]. The idea of acquiring tilt-series at equal slope increments and then combining the PPFFT with iterative algorithms for tomographic reconstructions was first proposed by Miao *et al*. in 2005[21].

II.B. The EST Method

Although the PPFFT and its inverse provide an algebraically exact way to do fast Fourier transform between the Cartesian and pseudopolar grids, three difficulties limit its direct application to tomographic reconstruction. First, to accurately invert the Fourier data using the PPFFT, knowledge of 2N data points along the 2N equally-sloped lines are needed[34]. This requirement of a large number of projections is not desirable in experiment due to radiation dose or technical restrictions. Second, the pseudopolar grid points past the resolution circle (indicated by the dotted circle in Fig. 1) cannot be experimentally determined[21] and, consequently, exact reconstructions through the inverse PPFFT are not possible. Third, in order to enhance the image quality and reduce radiation dose, the physical constraints and mathematical regularizations have to be applied in the image reconstruction, which requires the use of iterative algorithms.

To overcome these difficulties, the EST method was developed, which iterates back and forth between real and Fourier space[21-26]. The algorithm starts with padding each projection with zeros and calculating its oversampled Fourier slice in the pseudopolar grid (red lines in Fig. 2 top-right). The oversampling concept (*i.e.* sampling the Fourier slice at a frequency finer than the Nyquist interval) has been widely used to solve the phase problem in coherent diffraction imaging[36-38]. In the EST method, oversampling does not provide extra information about the object, but allows the use of iterative algorithms to extract the correlated information among different projections. In the first iteration, the grid points outside the resolution circle and on the missing projections (blue lines in Fig. 2 top-right) are set to zero. The algorithm then iterates back and forth between real and Fourier space by using the PPFFT. As shown in Fig. 2, the jth iteration consists of the following 6 steps:

i) Apply the adjoint transform to the Fourier-space slices $F_j(\vec{k})$, and obtain a real-space image, $f_j(\vec{r})$ (Fig. 2 bottom-right). Here the adjoint PPFFT instead of the inverse PPFFT is used because the former is implemented through a conjugate gradient method and can be computed much faster than the latter without compromising the accuracy [24].

ii) Derive a new object, $f_j^r(\vec{r})$, by applying mathematical regularizations to $f_j(\vec{r})$. In our reconstructions, we applied the non-local total variation regularization[29] once in every other iteration. The nonlocal total variation regularization is defined as:

$$J_W(f) = \int \sqrt{\int \left[f(p_1) - f(p_2) \right]^2 w(p_1, p_2) dp_1 dp_2} \tag{4}$$

Where the weight function $w(p_1, p_2)$ describing the similarity between the patches around different pixels p_1 and p_2. The object is regularized by minimizing:

$$\min_f J_w(f) + \frac{\lambda}{2} \left\| f - f_j \right\|^2 \tag{5}$$

This is not performed in the last iteration so that the final reconstruction is consistent with the measured data.

iii) A support is determined based on the zero padding of the projections. Outside the support, $f_j^r(\vec{r})$ is set to zero and inside the support, the negative values of $f_j^r(\vec{r})$ are set to zero as a physical constraint. A new image is obtained, defined as $f_j^{'}(\vec{r})$ (Fig. 2 bottom-left).

iv) Apply the PPFFT to $f_j^{'}(\vec{r})$ and obtain updated Fourier-space slices, $F_j^{'}(\vec{k})$ (Fig.2 top-left);

v) Obtain the Fourier slices for the (j+1)th iteration, (Fig. 2 top-right), by replacing $F_j^{'}(\vec{k})$ with the measured Fourier slices (red lines in Fig. 2). The grid points outside the resolution circle and on the missing Fourier slices remained unchanged.

vi) An error metric is calculated,

$$Error = \frac{\sum_k \left| F_j^{'}(\vec{k}) - F(\vec{k}) \right|_{k \le R}}{\sum_k \left| F_j^{'}(\vec{k}) + F(\vec{k}) \right|_{k \le R}} \tag{6}$$

where $F(\vec{k})$ represents the measured Fourier slices, $F_j^{'}(\vec{k})$ is the calculated Fourier slices in the jth iteration, and R is the radius of the resolution circle.

In our reconstructions, the algorithm is automatically terminated when the error becomes stabilized after about 20 iterations.

II.C. Data Acquisition

The data sets were acquired from a Siemens SOMATOM Sensation 64 scanner with axial mode on and only central slice was selected for reconstruction. As the scanner employs fan beam geometry, a rebinning step was performed prior to initiating the algorithm in order to transform the fan beam projections to parallel projections along equally-sloped lines of the pseudopolar gird. Since the scanner utilizes a flying focal spot (FFS) technology to increase detector sampling, the raw projections were interlaced and corrected prior to rebinning[39].

II.C.1. Phantom Studies

The Siemens image quality phantom (EMMA) is used to quantify the amount of CT dose reduction achievable by the EST method. The phantom contains resolution inserts to measure the image resolution (Fig. 3a), and contrast inserts to measure the image contrast (Fig. 3b-c). The resolution inserts, consisting of air, start at a resolution of 0.067 line pair per mm in group 1, to a resolution of 1 line pair per mm in group 11. The contrast inserts contain 8 different sets of cylindrical regions of varying contrast and size. The level of contrast is defined by the normalized electron density ratios (relative to solid water background): 1.01 (1% signal), 1.03 (3% signal), 1.05 (brain), 1.07 (liver), 1.09 (inner bone), 1.17 (acrylic), 1.48 (bone), and 0.001 (air), respectively for the regions labeled 1-8. The EMMA phantom was systematically scanned at different flux settings, ranging from a maximum of 583 mAs to a minimum of 39 mAs. All scans are performed under axial mode with the tube current modulation off and the voltage set to 120kVp. The scanner (FBP) reconstructions are performed with a standard uncropped ramp filter in conjunction with cubic interpolation for the back projection process. The EST reconstructions are computed by using the iterative algorithm described in Methods II.B.

II.C.2. Patient Studies

To further quantify the radiation dose reduction of medical CT in clinical environment with the EST method, a pediatric patient data set consisting of a cranial scan of an anonymous 8 year old boy is used. The scan was acquired under axial mode with a voltage of 120kVp and a flux setting of 140mAs. However, unlike the phantom studies, it is not possible to acquire repeated scans of the patient at different flux settings due to radiation dose concerns. To address this issue, we implement an algorithm to simulate low dose patient data based on existing scans[40,41]. Using this algorithm and the pediatric patient data set with a flux setting of 140 mAs, we generate CT scans at 39 mAs, the lowest possible flux setting of the Siemens Sensation SOMATOM 64 scanner, and 20 mAs, which is about 15% of the radiation dose for the original data set. Both the FBP and EST reconstructions are computed in the same manner as the phantom studies.

II.D. Evaluation Methods

We perform quantitative comparisons between the EST and the FBP reconstructions. In the phantom studies, the contrast and resolution inserts are used to evaluate the image contrast and image resolution at different flux levels. In both phantom and patient studies, quantitative comparisons are done by measuring the mean values and their standard deviation at various contrast regions to calculate the SNRs and the CNRs, defined as

$$\begin{aligned} SNR &= Mean(I_{ROI}) / Std(I_{ROI}) \\ CNR &= \left| Mean(I_{ROI_1}) - Mean(I_{ROI_2}) \right| / [0.5 \times (Std(I_{ROI_1}) + Std(I_{ROI_2}))] \end{aligned} \tag{7}$$

where I_{ROI} represents the pixel values in the region of interest (ROI).

III. RESULTS

III.A. Quantification of the Image Contrast

The detectability of low contrast features is one of the important criteria in low dose reconstructions, especially when using iterative algorithms. We have quantified the image contrast and quality of the EST and FBP reconstructions at different flux settings by using the medium and low contrast inserts of the EMMA phantom. Figures 4a-d show the FBP reconstructions at 583mAs, 140mAs, 39mAs and EST at 39mAs of the medium contrast insert, respectively. This inserts consist of 4 different sets of the cylinders, and the zoomed views of the lowest contrast set of the cylinders (9% signal) are shown in Fig. 4e-h. Compared to the FBP reconstructions at 140mAs and 39mAs, the EST reconstruction at 39mAs (Figs. 4d and h) exhibits better image quality and is more consistent with the reference reconstruction (FBP at 583mAs). As indicated by the arrows in the zoomed views (Fig. 4e-h), the smallest cylinder (3mm in diameter) is more visible in the 39mAs EST reconstruction than the 140 mAs FBP reconstruction. The SNRs and the CNRs were also calculated for the largest diameter cylinder (indicated in Figs. 4e-h). The SNRs and CNRs of the 39mAs EST reconstruction outperform all FBP ones, including the 583 mAs reference reconstruction. Fig. 5 shows the reconstruction images for the low contrast inserts of EMMA phantom. The overall quality of the 39 mAs EST reconstruction (Fig. 5d) is in good agreement with that of 583 mAs FBP (Fig. 5a), while the 140 mAs (Fig. 5b) and 39 mAs (Fig. 5c) FBP reconstructions are degraded by noise. Figures 5e-h show the zoomed view of the second highest contrast set of the cylinders (5% signal). The second smallest cylinder (5mm in diameter), indicated by arrows, is visible in the 583 mAs FBP and 39 mAs EST reconstructions, but becomes noisy in 140 mAs FBP and almost invisible in 39 mAs FBP. The SNRs and CNRs of the 39 mAs EST reconstruction are higher than those of all the FBP reconstructions.

III.B. Quantification of the Image Resolution

We quantified the image resolution of the FBP and EST reconstructions by using the resolution inserts of the EMMA phantom. Figures 6a-d show bar groups 10 and 11 in the resolution insert obtained from the 583mAs FBP, 140mAs FBP, 39mAs FBP, and 39mAs EST reconstructions, respectively. The smallest bar group 11 (1 line pair per mm) is not clearly discernable, but the second smallest bar group 10 (0.8 line pairs per mm) is visible in all reconstructions. In contrast to FBP reconstructions at 140 mAs and 39 mAs, in which noise degrades the geometrical fidelity of the bars as sharp rectangular objects, the 39mAs EST reconstruction (Fig. 6d) maintains a noise-free appearance similar to the 583mAs FBP reconstruction (Fig. 6a).

III.C. Pediatric Patient Data

Figures 7a-e show the results for a slice of the patient reconstructed at various low flux settings by FBP and EST. Visually it is noted that the low-dose EST reconstructions at 39 mAs and 20 mAs contain noise characteristics similar to FBP at 140 mAs, while the image quality of the low-dose FBP reconstructions (39 mAs and 20 mAs) are degraded by noise. This is more clearly illustrated in Figs. 7f-j which show zoomed images of a representative region with fine and low-contrast structures. In the area delineated by dotted ellipses, it is visible that some low-contrast features are significantly deteriorated in the low-dose FBP reconstructions. On the other hand, the EST 39 mAs reconstruction (Figs. 7c and h) is in good agreement with FBP at 140 mAs (Figs. 7a and f), while some geometrical inconsistencies can be noted in EST at 20 mAs. To quantify the EST reconstructions, the SNR and CNR in the regions indicated by a square in Fig. 7f are calculated. As indicated in Figs. 7f-j, the SNR and CNR of EST at 39 mAs are better than those of FBP at 140 mAs. A reconstruction of a second slice of the patient at a different anatomic region results in similar conclusion (Fig. 8). As more clearly illustrated in the zoomed regions in Fig. 8f-j, the fine features of the EST 39 mAs reconstruction are in good agreement with FBP at 140 mAs.

IV. CONCLUSION

Using the EMMA imaging quality phantom and a pediatric patient data acquired from a clinical CT scanner, we have demonstrated that the 39mAs EST reconstruction produces comparable or better image quality, resolution and contrast than the 140mAs FBP reconstruction. As the radiation dose is linearly proportional to the x-ray flux, our results suggest that EST enable a reduction of the CT dose by about 70% without compromising the image quality and accuracy. While we demonstrate the radiation dose reduction by using fan-beam CT data, the EST method can also be extended to circular/helical cone-beam geometry. Our recent studies have indicated that by using the rebinning process[42-45], circular/helical cone-beam projections can be used to calculate parallel projections along equally-sloped lines of the pseudopolar grid. A 3D object can then be reconstructed from the parallel projection using the iterative EST method. This work will be presented in a follow-up paper.

Compared to other iterative algorithms, EST takes advantage of the unique features in both real and Fourier space iterative algorithms by i) utilizing the algebraically exact and efficient PPFFT, ii) improving the computational speed as the PPFFT has the same computation complexity as the FFT, iii) eliminating the necessity for interpolation in Fourier space, and iv) searching for a global minimum, not only strictly consistent with the measured data but also satisfying the physical constraints and mathematical regularization. Due to these unique features, it is anticipated that the EST method can be applied not only to medical CT[1-3,20], but also other tomography fields[22,23,26,37].

Acknowledgement

We thank Henry Huang for stimulating discussion. This work was partially supported by UC Discovery/TomoSoft Technologies grant IT107-10166, and National Institutes of Health grant GM081409-01A1. Stanley Osher was supported by NSF grants DMS0835863 and DMS0914561.

References

[1]J. Hsieh, "*Computed Tomography: Principles, Design, Artifacts, and Recent Advances*," 2nd ed. (Wiley, Washington, 2009).

[2]A.C. Kak, and M. Slaney, *Principles of Computerized Tomographic Imaging*. (SIAM, Philadelphia, 2001).

[3]T. M. Buzug, *Computed Tomography: from photons statistics to modern cone-beam CT*. (Springer, Berlin, 2008).

[4]A. Berrington de Gonzalez, et al. "Projected cancer risks from computed tomographic scans performed in the United States in 2007," Arch. Intern. Med. **169**, 2071-2077 (2009).

[5]R. Smith-Bindman, et al. "Radiation dose associated with common computed tomography examinations and the associated lifetime attributable risk of cancer," Arch. Intern. Med. **169**, 2078-2086 (2009).

[6]R.F. Redberg, "Cancer risks and radiation exposure from computed tomographic scans," Arch. Intern. Med. **169**, 2049-2050 (2009).

[7]R.H. Fazel, et al. "Exposure to low-dose ionizing radiation from medical imaging procedures," N. Engl. J. Med. **361**, 849-857 (2009).

[8]A.J. Einstein, et al. "Radiation dose and cancer risk estimates in 16-slice computed tomography coronary angiography," J. Nucl. Cardio. **15**, 232-240 (2008).

[9]S. Kim, T.Yoshizumi, D.P. Frush, G. Toncheva, F.F. Yin, “Radiation dose from cone beam CT in a pediatric phantom: risk estimation of cancer incidence,” AJR Am J Roentgenol. **194**, 186-190 (2009).

[10]Annual report from the National Council on Radiation Protection & Measurements. <www.ncrponline.org/PDFs/NCRP_2009_Ann_Report.pdf> (2009).

[11]E. Candes, J. Romberg, T. Tao, “Exact signal reconstruction from highly incomplete frequency information,” IEEE Trans. Inf. Theory. **52**, 489–509 (2006).

[12]G.H. Chen, J. Tang, and S. Leng, “Prior image constrained compressed sensing (PICCS): a method to accurately reconstruct dynamic CT images from highly undersampled projection data sets,” Med. Phys. **35**(2), 660-3, (2008).

[13]E.Y. Sidky, and X. Pan, “Image reconstruction in circular cone-beam computed tomography by constrained, total-variation minimization,” Phys. Med. Biol. **53**(17), 4777-807, (2008).

[14]H. Yu, and G. Wang, “Compressed sensing based interior tomography,” Phys. Med. Biol. **54**(9), 2791–2805, (2009).

[15]G.H. Chen, et al., “Temporal resolution improvement using PICCS in MDCT cardiac imaging,” Med. Phys. **36**(6), 2130-35 (2009).

[16]J.C. Ramirez-Giraldo, et al., “Nonconvex prior image constrained compressed sensing (NCPICCS): Theory and simulations on perfusion CT,” Med. Phys, **38**(4), 2157-67 (2011).

[17]L. Ritschl, et al, “Improved total variation-based CT image reconstruction applied to clinical data,” Phys. Med. Biol. **56**(6), 1545-61(2011).

[18]L.A. Feldkamp, L.C. Davis, and J.W. Kress, “Practical cone-beam algorithm,” J. Opt. Soc. Am. B: Opt. Phys. 1(6), 612-9, (1984).

[19]X. Pan, E.Y. Sidky, M. Vannier, Why do commercial CT scanners still employ traditional, filtered back-projection for image reconstruction?. Inverse Problems **25**, 123009 (2009).

[20]G. T. Herman, *Fundamentals of Computerized Tomography: Image reconstruction from projection*, 2nd ed. (Springer, New York, 2009).

[21]J. Miao, F. Förster, O. Levi, “Equally sloped tomography with oversampling reconstruction,” Phys. Rev. B. **72**, 052103 (2005).

[22]J. Miao, C.C. Chen, C. Song, Y. Nishino, Y. Kohmura, T. Ishikawa, D. Ramunno-Johnson, T.K. Lee, S.H. Risbud, “Three-Dimensional GaN-Ga_2O_3 Core Shell Structure Revealed by X-ray Diffraction Microscopy”, Phys. Rev. Lett. **97**, 215503 (2006).

[23]E. Lee, B.P. Fahimian, C.V. Iancu, C. Suloway, G.E. Murphy, E.R. Wright, D. Castaño-Díez, G.J. Jensen, and J. Miao, “Radiation dose reduction and image enhancement in biological imaging through equally-sloped tomography,” J. Struct. Biol. **164**(2), 221-227, (2008).

[24]Y. Mao, B.P. Fahimian, S. Osher, J. Miao, “Development and Optimization of Regularized Tomographic Reconstruction Algorithms Utilizing Equally-Sloped Tomography,” IEEE Trans Image Process. **19**(5), 1259 – 1268, (2010).

[25]B.P. Fahimian, Y. Mao, P. Cloetens, J. Miao, “Low dose x-ray phase-contrast and absorption CT using Equally-Sloped Tomography,” Phys. Med. Biol. **55**, 5383-5400 (2010).

[26]H. Jiang, C. Song, C.-C. Chen, R. Xu, K.S. Raines, B.P. Fahimian, C. Lu,. T.-H. Lee, A. Nakashima, J. Urano, T. Ishikawa, F. Tamanoi, J. Miao, “Quantitative 3D Imaging of Whole, Unstained Cells by Using X-ray Diffraction Microscopy,” Proc. Natl. Acad. Sci. USA. **107**, 11234–11239 (2010).

[27]S. Osher, M. Burger, D. Goldfarb, J. Xu, W. Yin, “An iterative regularization method for total variation-based image restoration,” Multiscale Model Simul. **4**, 460-489 (2005).

[28]A. Buades, B. Coll, J.M. Morel, "A review of image denoising algorithms, with a new one," Multiscale Model. Simul. **4**, 490–530 (2005).

[29]G. Gilboa and S. Osher, "Nonlocal operators with applications to image processing," Multiscale Model. Simul. **7**, 1005–1028 (2008).

[30]S. Matej, J.A. Fessler, I.G. Kazantsev, "Iterative tomographic image reconstruction using Fourier-based forward and back-projectors," IEEE Trans. Med. Imaging. **23**, 401-412 (2004).

[31]Y. Zhang-O'Connor and J.A. Fessler, "Fourier-based forward and back-projectors in iterative fan-beam tomographic image reconstruction," IEEE Trans. Med. Imag. **25**, 582-9 (2006).

[32]W.L. Briggs and V.E. Henson, *The DFT: an owner's manual for the discrete Fourier transform.* 3rd ed. (SIAM, Philadelphia, 1995).

[33]R.M. Mersereau and A.V. Oppenheim, "Digital reconstruction of multidimensional signals from their projections," Proc. IEEE. 62 1319–38 (1974).

[34]A. Averbuch, et al., "A Framework for Discrete Integral Transformations I—The Pseudopolar Fourier Transform," SIAM Journal on Scientific Computing. **30**(2), 785-803, (2008).

[35]D.H. Bailey, and P.N. Swarztrauber, "The fractional Fourier transform and applications," SIAM Review. 33(3), (1991).

[36]J. Miao, P. Charalambous, J. Kirz and D. Sayre, "Extending the methodology of X-ray crystallography to allow imaging of micrometre-sized non-crystalline specimens," Nature. **400**, 342-344 (1999).

[37]J. Miao, T. Ishikawa, T. Earnest, Q. Shen, "Extending the Methodology of X-ray Crystallography to Allow Structure Determination of Non-Crystalline Materials, Whole Cells and Single Macromolecular Complexes," Annu. Rev. Phys. Chem. **59**, 387–409 (2008).

[38]K.S. Raines, S. Salha, R.L. Sandberg, H. Jiang, J.A. Rodríguez, B.P. Fahimian, H.C. Kapteyn, J. Du and J. Miao, "Three-dimensional structure determination from a single view," Nature. **463**, 214-217 (2010).

[39]Y. Kyriakou, M. Kachelriess, M. Knaup, J.U. Krause, W.A. Kalender, "Impact of the z-flying focal spot on resolution and artifact behavior for a 64-slice spiral CT scanner," Eur. Radiol. 16, (6), 1206-15, (2006).

[40]P. Massoumzadeh, et al., "Validation of CT dose-reduction simulation," Med. Phys. **36**(1) 174-89 (2009).

[41]B.R. Whiting, et al., "Properties of preprocessed sinogram data in x-ray computed tomography," Med. Phys. **33**(9), 3290-303 (2006).

[42]F. Noo, M. Defrise, R. Clackdoyle, "Single-slice rebinning method for helical cone-beam CT," Phys. Med. Biol. 44(2), 561-70, (1999).

[43]J. Hsieh, and X. Tang, "Tilted cone-beam reconstruction with row-wise fan-to-parallel rebinning," Phys. Med. Biol. **51**(20), 5259-76, (2006).

[44]M. Kachelriess, S. Schaller, W.A. Kalender, "Advanced single-slice rebinning in cone-beam spiral CT," Med. Phys. **27**(4), 754-72, (2000).

[45]S. Schaller, et al., "New, efficient Fourier-reconstruction method for approximate image reconstruction in spiral cone-beam CT at small cone angles," Proc. of SPIE, **3032**, 213-224(1997).

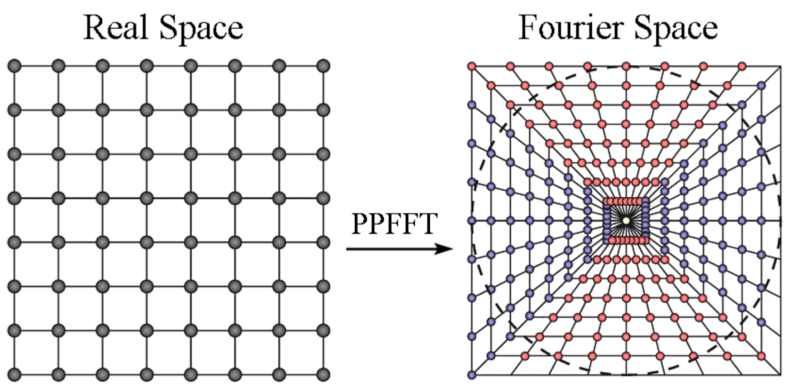

FIG. 1. Geometrical representation of a Cartesian and pseudopolar grids, related by the algebraically exact PPFFT. The dotted circle represents the resolution circle.

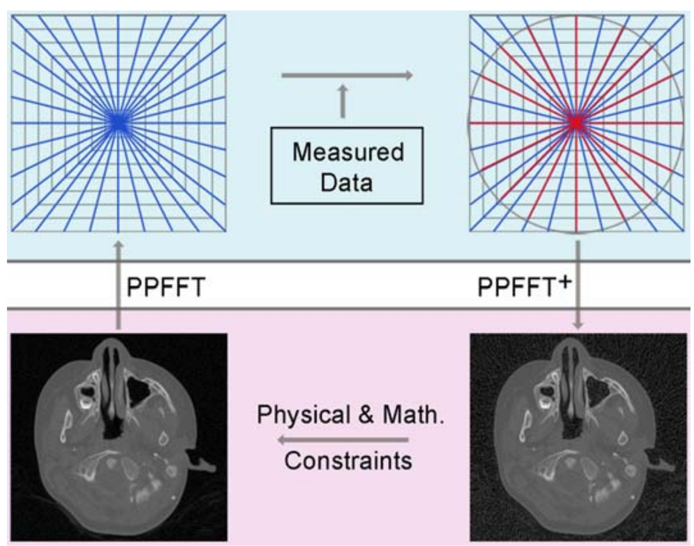

FIG. 2. Schematic of the EST method which iterates back and forth between real and Fourier space. The forward transform from a Cartesian grid in real space (bottom-left) to a pseudopolar grid in Fourier space (top-left) is performed by the pseudopolar fast Fourier transform (PPFFT). The backward step from Fourier space to real space is performed by the adjoint transform of the PPFFT (PPFFT^{+}), .In each iteration, physical and mathematical constraints are enforced in real

space (bottom-right), while measured data (red lines in top-right) is applied in Fourier space. An error metric is used to monitor the convergence of the iterative algorithm.

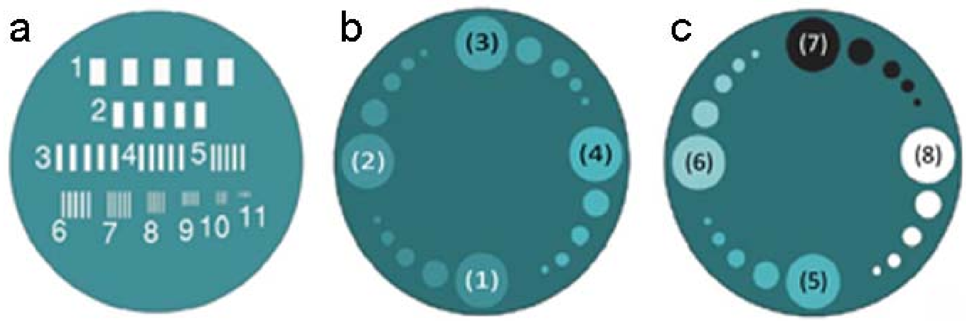

FIG. 3. Three different slices of Siemens' image quality phantom (EMMA). (a) Resolution insert (b) Low contrast insert (c) Medium contrast insert .

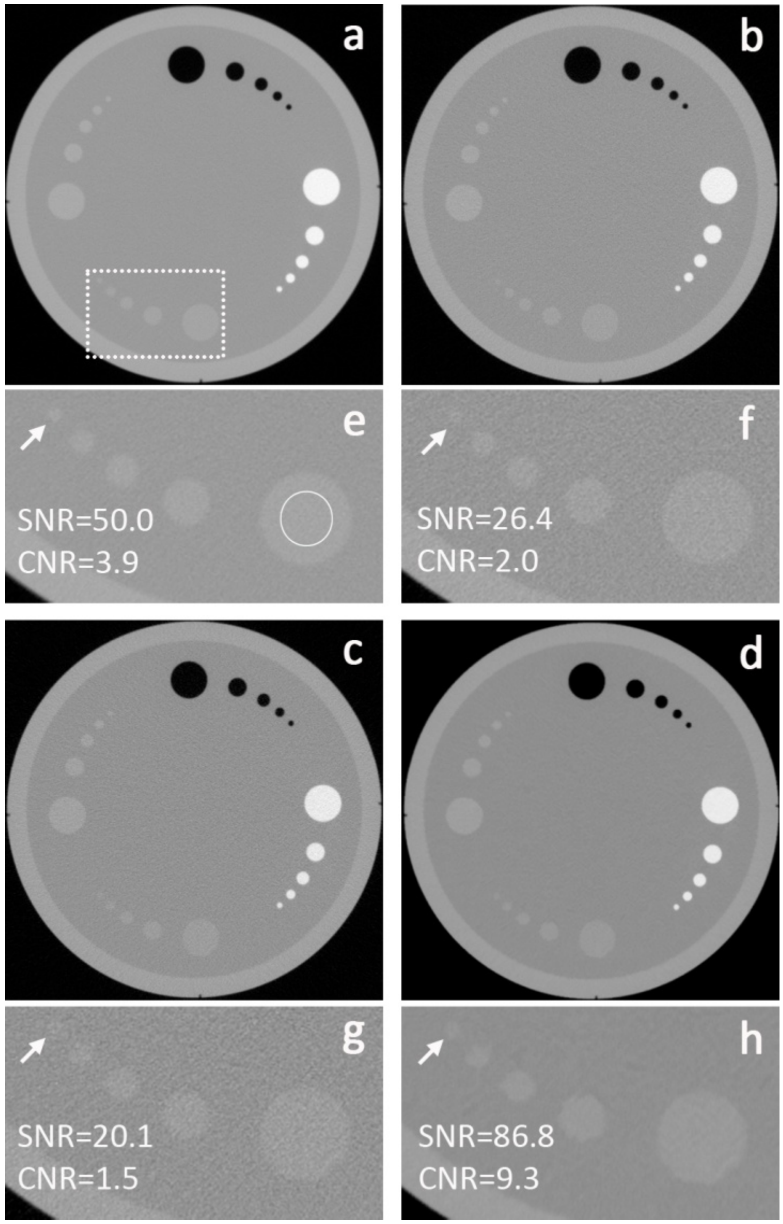

FIG. 4. Comparative reconstructions of the medium contrast insert of the EMMA phantom. Reconstructions of (a) 583 mAs FBP, (b) 140 mAs FBP, (c) 39 mAs FBP, and (d) 39 mAs EST. (e)-(h) Zoomed images of the 9% signal region from (a)-(d), where the SNRs and CNRs were calculated for the largest diameter cylinder, indicated by the circle in (e).

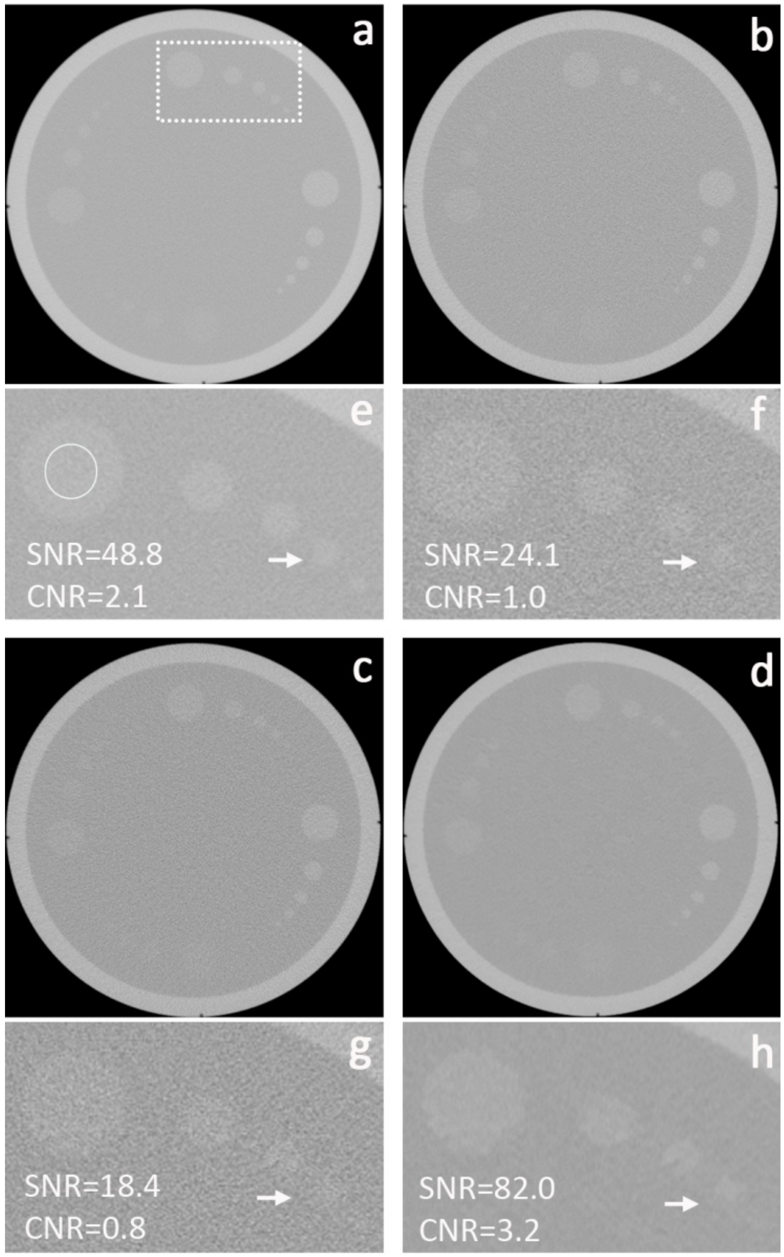

FIG. 5. Comparative reconstructions of the low-contrast insert of EMMA phantom. (a) 583 mAs FBP, (b) 140 mAs FBP, (c) 39 mAs FBP and (d) 39 mAs EST. (e)-(h) Zoomed views of the 5% signal region (dotted square). The 5mm diameter cylinder is indicated by arrows. The SNRs and CNRs of the circled region, labled in (e), were calculated for all the reconstructions.

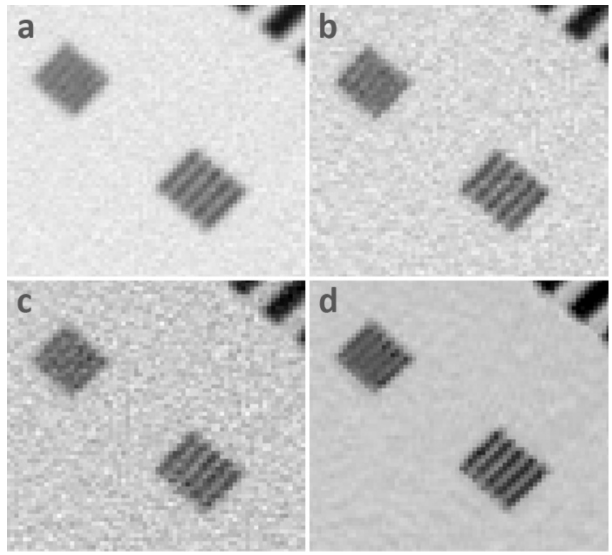

FIG. 6. Comparative reconstructions of the resolution insert of the EMMA phantom. Zoomed images of two smallest bar groups 10 & 11 for the reconstructions of (a) 583 mAs FBP, (b) 140 mAs FPB, (c) 39 mAs FBP, and (d) 39 mAs EST.

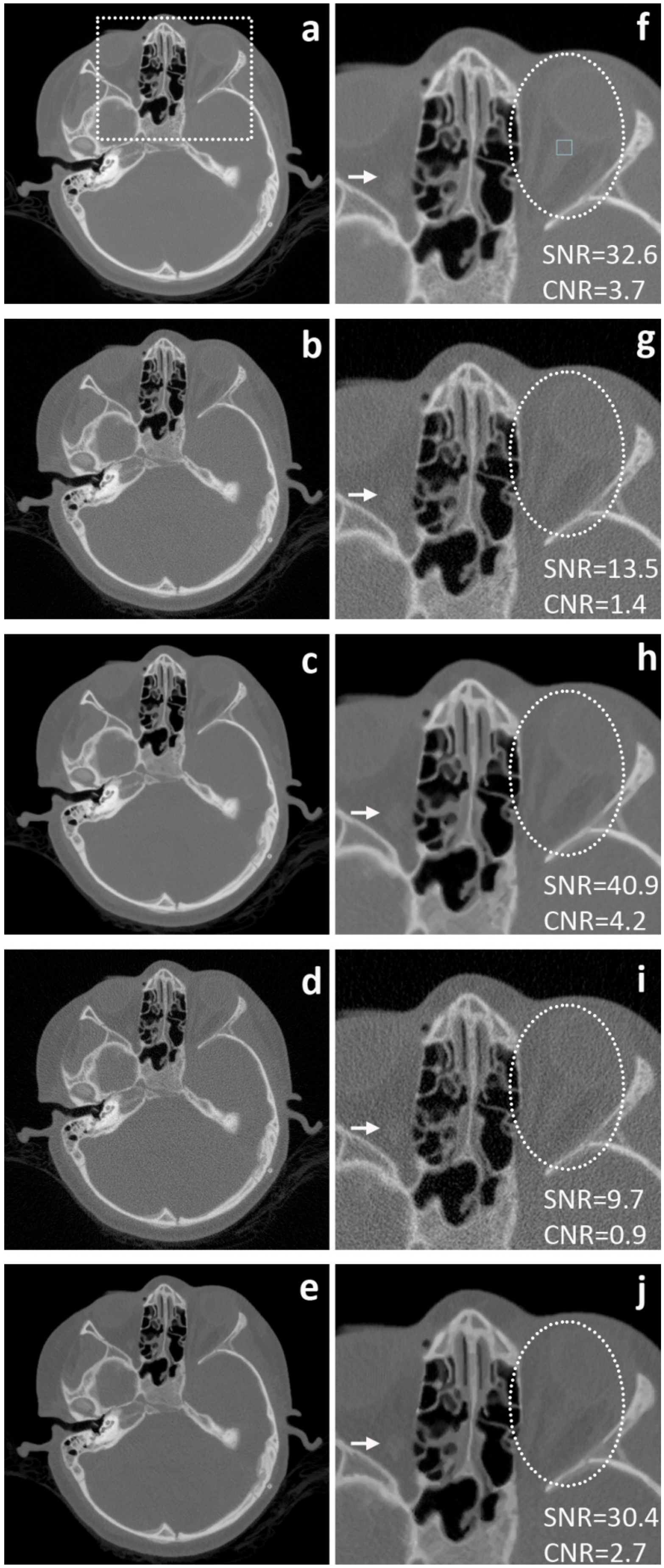

a
f
SNR=32.6
CNR=3.7
b
g
SNR=13.5
CNR=1.4
c
h
SNR=40.9
CNR=4.2
d
i
SNR=9.7
CNR=0.9
e
j
SNR=30.4
CNR=2.7

FIG. 7. Comparative reconstructions of a head slice from an anonymous pediatric patient. (a-e) Whole slice reconstructions for 140 mAs FBP, 39 mAs FBP, 39 mAs EST, 20 mAs FBP and 20 mAs EST, respectively. (f-j) The corresponding zoomed images of a representative region (the dotted square) with fine and low-contrast structures. The SNR and CNRs were calculated in the regions indicated by the square in (f). The while arrows point to a fine feature.

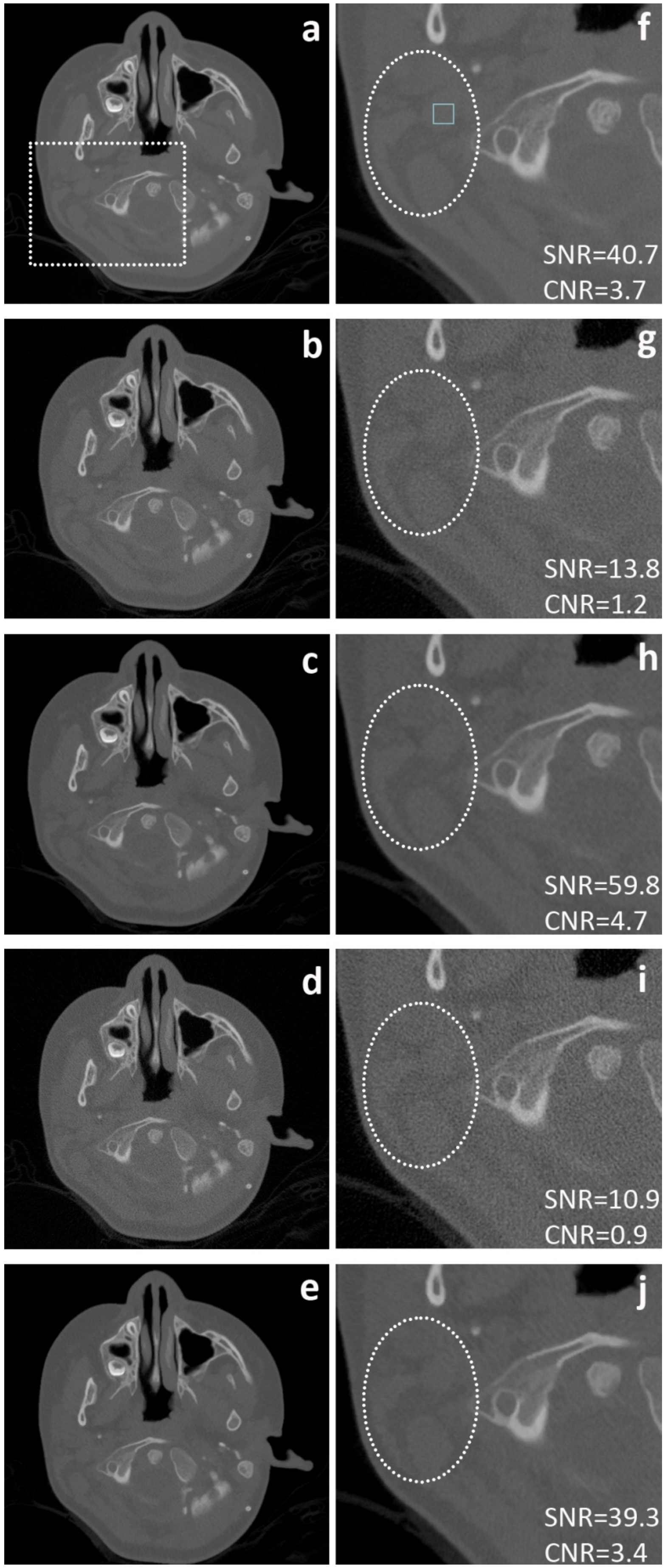
a
f
SNR=40.7
CNR=3.7
b
g
SNR=13.8
CNR=1.2
c
h
SNR=59.8
CNR=4.7
d
i
SNR=10.9
CNR=0.9
e
j
SNR=39.3
CNR=3.4

FIG. 8. Comparative reconstructions of another head slice from the same pediatric patient data set.(a-e) Whole slice reconstructions for 140 mAs FBP, 39 mAs FBP, 39 mAs EST, 20 mAs FBP and 20 mAs EST, respectively. (f-j) The corresponding zoomed images of a representative region (the dotted square) with fine and low-contrast structures. The SNR and CNRs were calculated in the regions indicated by the square in (f).